

# The effect of hydrogen on the deformation of pearlite in steels

**Julie Cairney** (✉ [julie.cairney@sydney.edu.au](mailto:julie.cairney@sydney.edu.au))

The University of Sydney <https://orcid.org/0000-0003-4564-2675>

**Ranming Niu**

University of Sydney <https://orcid.org/0000-0001-8190-552X>

**Hanyu Li**

University of Sydney

**Pang-Yu Liu**

University of Sydney <https://orcid.org/0000-0003-1583-3155>

**Patrick Burr**

University of New South Wales <https://orcid.org/0000-0003-4796-9110>

**Yi Feng**

China Automotive Engineering Research Institute Co., Ltd.

**Hung-Wei Yen**

National Taiwan University <https://orcid.org/0000-0002-7885-938X>

**Mintu Ma**

China Automotive Engineering Research Institute Co., Ltd

**Aimin Guo**

CITIC Metal Co.

**Hongzhou Lu**

CITIC Metal Co.

**Yi-Sheng Chen**

University of Sydney <https://orcid.org/0000-0002-2607-4388>

---

**Physical Sciences - Article**

**Keywords:**

**Posted Date:** February 14th, 2022

**DOI:** <https://doi.org/10.21203/rs.3.rs-1325909/v1>

**License:**   This work is licensed under a Creative Commons Attribution 4.0 International License.

[Read Full License](#)

# Abstract

Hydrogen embrittlement in steel gas infrastructure is a serious challenge for the use of hydrogen energy for global decarbonization. Steel gas pipelines contain a significant fraction of pearlite, which consists of lamellar cementite in ferrite. How exactly hydrogen affects deformation and failure in this structure, and hence the role that pearlite plays in embrittlement, is not well understood. Here we have studied the behavior of hydrogen around the cementite–ferrite interface, the defining microstructural feature in pearlite. Our micromechanical testing results show softening in the ferrite adjacent to the interface, consistent with hydrogen-enhanced local plasticity, rather than interfacial weakening. Atom probe tomography (APT) observations of hydrogen at the interface show no evidence of trapping at the cementite–ferrite interface, instead hydrogen trapping in pearlite occurs in the cementite bulk. Density functional theory calculations, accounting for the configuration of the lattice defects and local interfacial misfits, are consistent with the experimental observations. These findings explain how hydrogen leads to degradation in pearlite. This information is critical for the development of next-generation pipeline materials that can better withstand hydrogen embrittlement.

# Full Text

Decarbonization is required to save the world from the threats of climate change. The use of hydrogen as a clean fuel to reduce our dependence on fossil fuel energy sources is one of the most promising decarbonization strategies. Under the guidance of the International Energy Agency, many major economies have incorporated hydrogen into their national energy strategies, including USA, EU, UK, Japan, Korea, Australia, and Canada<sup>1</sup>. A common assumption in these campaigns is the ability to leverage existing natural gas infrastructure for hydrogen transmission, allowing for cost-effectiveness and timely implementation without major infrastructural renovation.

However, existing gas infrastructure is comprised mainly of steel, and it is well established that gaseous hydrogen is absorbed by steel, reducing the toughness, and potentially leading to catastrophic failure. This effect is known as ‘hydrogen embrittlement’ (HE)<sup>2</sup>. This is an enormous concern, since hydrogen is flammable, even explosive, and leakage due to the structural failure of hydrogen pipes or vessels poses a safety risk<sup>3</sup>. As such, it is paramount to understand how hydrogen leads to HE in gas pipeline steels, both for risk mitigation for existing infrastructure, and to provide guidance for the development of future hydrogen-safe alloys.

Conventional pipeline steels such as API X52 or X65 contain a characteristic pearlite microstructure (up to 20% in volume) that is comprised of lamellar cementite ( $\text{Fe}_3\text{C}$ ) in a body-centered cubic ferrite matrix<sup>4,5</sup>. Although it is an important phase in these steels, the role of hydrogen on the deformation behavior of this complex microstructure has been less well studied than the simpler phases in these alloys, such as ferrite<sup>2</sup>. HE in ferrite is attributed to two major causes: first, the presence of hydrogen in solution around dislocations in bulk ferrite (the Cottrell atmosphere) can reduce the elastic field required to overcome dislocation movement<sup>6,7</sup>, resulting in more active dislocations that increase the local plasticity and

weaken the local resistance to strain, leading to either hydrogen-enhanced localized plasticity (HELP) when hydrogen pre-exists in the bulk structure<sup>8</sup> or adsorption-induced dislocation emission (AIDE) when surface uptake is the major source of hydrogen<sup>9</sup>. Second, local accumulation of hydrogen solute can directly reduce the strength of interatomic bonds and lead to hydrogen-enhanced decohesion (HEDE)<sup>10</sup>. HEDE is generally accepted to be the cause of intergranular and interfacial failures<sup>2</sup>.

Pearlite contains both ferrite and a high proportion of cementite–ferrite interfaces, so it has the potential to be susceptible to both HELP (within the ferrite) and HEDE (at the interfaces). How deformation behavior changes in the presence of hydrogen is not well understood<sup>11</sup>. Valuable insights into deformation and failure can be gained from microscopic observations made together with in-situ straining. These are especially valuable where the tests can be carried out in custom environments such as high/low temperatures or under gas exposure<sup>11-17</sup>.

It would be even more powerful to be able to correlate material's micromechanical response to hydrogen with the exact distribution of hydrogen in microstructure, allowing an understanding of which part of the microstructure is responsible for the deformation that leads to embrittlement. The size and mobility of hydrogen atoms make it challenging to unambiguously observe hydrogen at a small length scale<sup>19</sup>. Recently, the development of cryogenic atom probe tomography (cryo-APT) has enabled atomic-scale hydrogen mapping<sup>20,21</sup>, opening up the possibility of comparing micromechanical properties and hydrogen distribution to comprehensively depict how hydrogen induces degradation in steels.

As well as understanding embrittlement mechanisms, there is also interest in understanding how hydrogen is trapped in pearlite<sup>22</sup>. This information is useful because introducing hydrogen traps to a microstructure to confine hydrogen at benign places is a promising strategy for enhancing HE resistance<sup>23</sup>. A clear understanding of hydrogen trapping in pipeline steels could lead to the design of next-generation materials that can better withstand HE and be safely used for hydrogen transport. Here, we use advanced microscopy to advance understanding of HE in pipeline steels by establishing: i) how hydrogen affects deformation (and hence embrittlement) and ii) hydrogen trapping, in pearlitic steel.

We used a model pearlitic steel (see Methods for details) with a high volume fraction of pearlite. The darker phase in Fig. 1a is the cementite and the lighter phase is the ferritic matrix. Transmission electron microscopy (TEM) was used to examine the structure. A bright field image taken along the [111] direction is shown in Fig. 1b. Selected area electron diffraction (SAED) (inset in Fig. 1b) confirmed that the cementite and ferrite have a specific orientation relationship,  $[110]_{\text{cementite}} // [112]_{\text{ferrite}}$ , known as the Isaichev relationship<sup>24</sup>. High-angle annular dark-field scanning transmission electron microscopy (HAADF-STEM) imaging (Fig. 1c) confirmed that the cementite–ferrite interface is coherent. Geometric phase analysis<sup>25</sup>, Fig. 1d, provided a lattice strain map of the interfacial area shown in Fig. 1c. The ferrite region indicated by the orange arrow is expanded compared to the relaxed ferrite (far left). The blue arrow indicates a compressed cementite region with a different level of strain compared to the bulk cementite in

the right of the figure, resulting from the lattice misfit between the two phases at this  $[110]_{\text{cementite}}//[112]_{\text{ferrite}}$  interface.

We also used APT to analyze the composition of the cementite in an as-received pearlitic specimen. A needle-shaped sample was fabricated that deliberately contained a cementite lamella angled close to  $45^\circ$  to provide an optimal combination of data yield and the spatial resolution of elemental mapping at the interface<sup>26</sup> (see Methods and Extended Data Fig. 1). The APT result is shown in Fig. 1e (Supplementary Video 1 for the animated version), where Fe and C atoms correspond to grey and blue dots, respectively. A 10 nm thick slice of data from the highlighted region of Fig. 1e is shown in Fig. 1f, and a 1-D concentration profile from the region highlighted in Fig. 1f along the direction of black arrow is provided in Fig. 1g. The carbon concentration measured in cementite (maximum 22 at. %) is slightly lower than might be expected for stoichiometric ( $\text{Fe}_3\text{C}$ ). The literature suggests that the quantification approach used here would be expected to provide a relatively accurate carbon content in APT<sup>27,28</sup> (see Extended Data Fig. 2 for ion labelling in the APT mass spectra). We thus attribute this carbon deficit to the presence of carbon vacancies in the cementite, consistent with other literature in which evidence was obtained through other techniques<sup>29</sup>.

To measure and observe the effect of hydrogen on deformation in pearlite and, specifically, around the cementite–ferrite interfaces, we conducted a series of in-situ compression tests on prefabricated micropillars (Fig. 2), 1  $\mu\text{m}$  in diameter and 3  $\mu\text{m}$  in height, prepared by a focused ion beam (FIB). The micropillars contained cementite lamellae angled close to  $45^\circ$  ( $\pm 5^\circ$ ) from the mechanical loading direction (Fig. 2a). This was achieved by using electron backscatter diffraction (EBSD) to select ferrite grains at the correct orientation (see Methods for details). After testing the uncharged micropillars, the entire specimen, with pre-fabricated micropillars, was electrolytically charged with hydrogen (see Methods). Hydrogen diffuses quickly and can easily escape from microscale specimens<sup>20,21</sup>, but the bulk specimen acts as a reservoir to supply additional hydrogen. To ensure that the specimens still contained sufficient hydrogen during our experiment, we conducted a series of thermal desorption analysis (TDA) experiments to establish a reference hydrogen content against time in vacuum (see Methods and Extended Data Fig. 5). These measurements suggest that approximately 137 mass part per billion (mppb) of hydrogen would remain in a specimen the size of ours at the start of the micro-compression tests (0.5 hours after hydrogen charging). 35 mppb of hydrogen would remain in the specimen at the completion of a set of micromechanical tests (4 hours after charging), which is still significantly more than an uncharged reference of 17 mppb.

Typical stress–strain curves from the uncharged and hydrogen-charged micropillars are shown in Fig. 2b. All the reported stress data has been converted to resolved shear stress by measuring the angle between cementite lamellae and the load axis. The hydrogen-charged samples consistently displayed different yield behavior to those that had not been charged, as seen in Fig. 2b. The yield stresses of uncharged and hydrogen-charged specimens are 0.93 and 0.53 GPa, respectively, suggesting that hydrogen lowers the strength of the micropillars by approximately 40%. The uncharged sample displays sudden bursts of

strain, that correspond drops in the stress; examples are labelled c-e in Fig. 2b<sup>30</sup>. The charged sample displayed a steadier deformation at a more consistent level of stress. Data from additional tests reproducing similar results can be found in Extended Data Fig. 4.

Images of the micropillars at various stages of deformation (marked in Fig. 2b) are shown in Figs. 2c–e (uncharged) and 2f–h (hydrogen charged). In the uncharged samples, we observed sudden shearing along the cementite–ferrite interface orientation on a limited number of planes (yellow arrows in Fig. 2d and 2d). Whereas in the hydrogen-charged samples, we observed a larger set of parallel deformation planes (yellow arrows in Fig. 2h) activating consequently and then operating simultaneously. The nature of the deformation is apparent in the videos (Supplementary Videos 2 and 3).

We prepared a cross-section of a hydrogen-charged micropillar perpendicular to the slip planes after deformation by using FIB/SEM. The cementite lamellae can be seen in Fig. 2i. All slip, as identified by surface ridges, occurred along planes parallel to the cementite lamellae. We then used FIB lift-out to prepare a cross-sectional TEM specimen from the sectioned micropillar. Fig. 2j is a bright field TEM image from a region close to the area highlighted by the red square in Fig. 2i. Fig. 2j shows that the ridge/slip (yellow broken line) in the hydrogen-charged specimen is only *near*, not *at*, the cementite–ferrite interface, which is different to observations of uncharged samples, which deform *at* the interfaces (See Extended Data Fig. 6).

The results suggest that hydrogen reduces the micropillar's strength by reducing the barrier to activate dislocation motion, consistent with the HELP model, rather than reducing the cohesion of a specific interface, as might be predicted by HEDE<sup>2</sup>. The ferrite-cementite interface lies along the {112} planes of ferrite (Fig. 1c), which is one of the primary slip systems of a body-centered cubic structure<sup>31</sup>. Hydrogen reduces the energy required for dislocation motion along this slip plane within the ferrite, reducing the strength, consistent with the HELP mechanism<sup>2</sup>.

To better understand the relationship between the deformation mechanisms in pearlite and the presence of hydrogen, we used cryo-APT to directly observe hydrogen around a cementite–ferrite interface (Fig. 3). The specimens were electrolytically charged with deuterium, similar to our previous work<sup>20,21</sup>, to distinguish the signal from artefacts that result from hydrogen in the vacuum chamber. Cryogenic sample transfer suppressed deuterium diffusion loss as the sample was loaded into the atom probe. Voltage-pulsed APT was used to minimize any signal from H<sub>2</sub> (no signal at 2 Da was observed in the uncharged specimens as per Extended Data Fig. 2). The 3-D atom map shown in Fig. 3a contains cementite lamella, which can be identified by the blue carbon atoms. Deuterium atoms are shown in red. Fig. 3b is a 10-nm thick slice extracted from the x-z plane marked by the broken line in Fig. 3a. We did not observe any deuterium enrichment/segregation at the cementite–ferrite interface. In fact, there appears to be a region of lower deuterium concentration in the ferrite in the vicinity of the interface. Fig. 3c is a 1-D concentration profile across the cementite lamella in the direction noted by the black arrow in Fig. 3a, which confirms that deuterium is present in both the cementite and the ferrite, but that a deuterium 'depletion zone' exists near the cementite–ferrite interface. This depletion zone is only few nanometers thick. We repeated the

experiment obtained a similar result, as shown in Extended Data Fig. 7 and Supplementary Video 4. In the animated dataset of Fig. 3 (Supplementary Video 5), it is apparent that the deuterium is not evenly distributed in the ferrite. Deuterium-enriched regions of the ferrite are aligned. We believe this irregular segregation of deuterium is associated with hydrogen enrichment in the vicinity of lattice defects as evidenced in our previous study<sup>21</sup>.

Our APT results have shown evidence of hydrogen trapping in 1) the cementite bulk and 2) at defects in ferrite. Our results differ from the work of Breen et al.<sup>32</sup> who also used cryo-APT for hydrogen mapping in pearlite, concluding that hydrogen trapping predominantly occurs within the cementite bulk but with additional slight segregation to at least some cementite–ferrite interfaces. There are several possible explanations for the difference in our findings. Here we used a pearlitic specimen that did not experience significant cold work after hot rolling, which is distinct to Breen et al.'s cold-drawn pearlitic wire specimens. This means that our specimen contains less accumulated defects at the cementite–ferrite interfaces. Breen et al.'s APT experiments used cold-drawn pearlitic wires with cementite lamellae aligned in the axial direction of their wires and APT tips. The spatial resolution in atom probe is higher in the analysis direction (the z-direction along the length of the tip)<sup>26</sup>, so it would be expected to be higher in the present work.

To understand the reason for the observed spatial distribution of hydrogen, we used density function theory (DFT) to calculate the relative hydrogen trapping potential in the proximity of the cementite–ferrite interface. The 1-D concentration profile of deuterium in Fig. 3c is expected to be related to the energy landscape for hydrogen migration and trapping around the interface. It is possible that this coherent cementite–ferrite interface (as shown in Fig. 1c) is a weaker trapping site for hydrogen than bulk cementite and ferrite, both of which have defects that can accommodate hydrogen solute atoms. We calculated the lattice misfit in for cementite and ferrite around a coherent interface, Fig. 1d. We also assume the presence of 6.25% carbon vacancies (1 vacancy per 16 carbon atoms, which is equivalent to an overall 1.47% deficiency of carbon to the  $\text{Fe}_3\text{C}$  cementite stoichiometry) in cementite as suggested by the literature<sup>29</sup> and as evidenced by the carbon deficit to  $\text{Fe}_3\text{C}$  stoichiometry seen in both Figs. 1f and 3c. Modelling details can be found in Methods.

We determined the relative potential energy of a hydrogen solute atom as a function of its distance to the cementite–ferrite interface, Fig. 4a. The gradient colors in Fig. 4a refer to the tension in ferrite (grey) and the compression in cementite (blue) near the interface. Details of the elastic strain calculation are presented in Methods. The black solid line in Fig. 4a suggests that hydrogen atoms have a lower potential (is more stable) in the region of ferrite that is under tension, so the hydrogen would be expected to segregate to this region. However, we also found that the solution energy of hydrogen in a defect-free cementite lattice is 0.11 eV lower than the ferrite under tension. This means that hydrogen atoms in the tensile region are attracted to the lower energy environment in cementite. We then consider the hydrogen potential of cementite with 6.25 at.% carbon vacancies as shown by the red broken line in Fig. 4. In this case, the potential of entry is enhanced to 0.3 eV since the carbon vacancies in cementite are strong

hydrogen traps<sup>33,34</sup>. These modelling results provides a rationale for the presence of a ~5 nm hydrogen depletion zone in ferrite (Figs. 3b and 3c), i.e. hydrogen atoms in this zone are drained to cementite where stronger trapping sites are available. Compression of the cementite lattice slightly reduces the hydrogen trapping energy near the interface, so when hydrogen atoms enter cementite, it would be expected to continue to penetrate into the cementite core rather than accumulating at the interface, consistent with the experimental data in Fig. 3. Note that that some carbides in ferrite (e.g. niobium carbide) have been shown to trap hydrogen<sup>21</sup> at their surface, which is able to be resolved by APT, but we did not find any evidence of such an effect in this pearlite.

DFT, APT, and micromechanics have led to a better understanding of hydrogen near the cementite–ferrite interface, illustrated in Fig. 4b. Hydrogen reduces the strength of pearlitic specimens, not by directly affecting the interface, but by promoting ferrite deformation. Hydrogen is attracted toward the cementite–ferrite interface due to the potential gradient created by the lattice misfit, but is attracted by the lower energy environment within the cementite, leaving a hydrogen depletion zone in the ferrite region near the interface. When hydrogen enters cementite, it can be strongly trapped in the cementite bulk, where the trapping potential is enhanced by carbon vacancies. A strain gradient in the cementite bulk further encourages incorporation of hydrogen into the cementite, consistent with our APT analysis. In summary, we clarify that i) lower yield stress in pearlite in the presence of hydrogen is the result of HELP, not HEDE, and ii) hydrogen trapping in this microstructure occurs in the cementite bulk, not at the cementite–ferrite interface.

## References

1. International Energy Agency, Global Hydrogen Review 2021, (2021)
2. Martin, M. L., Connolly, M. J., Delrio, F. W. & Slifka, A. J. Hydrogen embrittlement in ferritic steels. *Appl. Phys. Rev.* **7**, (2020).
3. Rhodes, R. Explosive Lessons in Hydrogen Safety. *NASA ASK Mag.* **41**, 46–50 (2011).
4. Wang, J. Q., Atrens, A., Cousens, D. R. & Kinaev, N. Microstructure of X52 and X65 pipeline steels. *J. Mater. Sci.* **34**, 1721–1728 (1999).
5. Ohaeri, E. G., Qin, W. & Szpunar, J. A critical perspective on pipeline processing and failure risks in hydrogen service conditions. *J. Alloys Compd.* **857**, (2021).
6. Robertson, I. M. *et al.* Hydrogen Embrittlement Understood. *Metall. Mater. Trans. B Process Metall. Mater. Process. Sci.* **46**, 1085–1103 (2015).
7. Lynch, S. Hydrogen embrittlement phenomena and mechanisms. *Corros. Rev.* **30**, 105–123 (2012).
8. Birnbaum, H. K. & Sofronis, P. Hydrogen-enhanced localized plasticity-a mechanism for hydrogen-related fracture. *Mater. Sci. Eng.* **176**, 191–202 (1994).
9. Lynch, S. P. Metallographic contributions to understanding mechanisms of environmentally assisted cracking. *Metallography* **23**, 147–171 (1989).

10. Oriani, R. A. A mechanistic theory of hydrogen embrittlement of steels. *Berichte der Bunsengesellschaft für Phys. Chemie* **76**, 848–857 (1972).
11. Toribio, J. HELP versus HEDE in progressively cold-drawn pearlitic steels: Between Donatello and Michelangelo. *Eng. Fail. Anal.* **94**, 157–164 (2018).
12. Lee, T. C., Dewald, D. K., Eades, J. A., Robertson, I. M. & Birnbaum, H. K. An environmental cell transmission electron microscope. *Rev. Sci. Instrum.* **62**, 1438–1444 (1991).
13. Greer, J. R. & De Hosson, J. T. M. Plasticity in small-sized metallic systems: Intrinsic versus extrinsic size effect. *Prog. Mater. Sci.* **56**, 654–724 (2011).
14. Kraft, O., Gruber, P. a., Mönig, R. & Weygand, D. Plasticity in Confined Dimensions. *Annu. Rev. Mater. Res.* **40**, 293–317 (2010).
15. Dewald, M. P. & Curtin, W. A. Multiscale modelling of dislocation/grain boundary interactions. II. Screw dislocations impinging on tilt boundaries in Al. *Philos. Mag.* **87**, 4615–4641 (2007).
16. Deng, Y., Hajilou, T., Wan, D., Kheradmand, N. & Barnoush, A. In-situ micro-cantilever bending test in environmental scanning electron microscope: Real time observation of hydrogen enhanced cracking. *Scr. Mater.* **127**, 19–23 (2017).
17. Xie, D. *et al.* Hydrogenated vacancies lock dislocations in aluminium. *Nat. Commun.* **7**, 1–7 (2016).
18. Asadipoor, M., Pourkamali Anaraki, A., Kadkhodapour, J., Sharifi, S. M. H. & Barnoush, A. Macro- and microscale investigations of hydrogen embrittlement in X70 pipeline steel by in-situ and ex-situ hydrogen charging tensile tests and in-situ electrochemical micro-cantilever bending test. *Mater. Sci. Eng. A* **772**, 138762 (2020).
19. Koyama, M. *et al.* Recent progress in microstructural hydrogen mapping in steels: quantification, kinetic analysis, and multi-scale characterisation. *Mater. Sci. Technol. (United Kingdom)* **33**, 1481–1496 (2017).
20. Chen, Y. S. *et al.* Direct observation of individual hydrogen atoms at trapping sites in a ferritic steel. *Science* **355**, 1196–1199 (2017).
21. Chen, Y. S. *et al.* Observation of hydrogen trapping at dislocations, grain boundaries, and precipitates. *Science* **367**, 171–175 (2020).
22. Yu, S. H. *et al.* Effects of lamellar structure on tensile properties and resistance to hydrogen embrittlement of pearlitic steel. *Acta Mater.* **172**, 92–101 (2019).
23. H.K.D.H. Bhadeshia. Prevention of Hydrogen Embrittlement in Steels. *ISIJ Int.* **56**, 24–36 (2016).
24. Zhou, D. S. & Shiflet, G. J. Ferrite: Cementite crystallography in pearlite. *Metall. Trans. A* **23**, 1259–1269 (1992).
25. Hÿtch, M. J., Snoeck, E. & Kilaas, R. Quantitative measurement of displacement and strain fields from HREM micrographs. *Ultramicroscopy* **74**, 131–146 (1998).\
26. Gault, B., Moody, M. P., Cairney, J. M. & Ringer, S. P. Atom Probe Microscopy. *Springer Science & Business Media.* (2012).

27. Thuvander, M. *et al.* Quantitative atom probe analysis of carbides. *Ultramicroscopy* **111**, 604–608 (2011).
28. Takahashi, J., Kawakami, K. & Kobayashi, Y. Quantitative analysis of carbon content in cementite in steel by atom probe tomography. *Ultramicroscopy* **111**, 1233–1238 (2011).
29. Voronin, V. I. *et al.* Composition of cementite in the dependence on the temperature. In situ neutron diffraction study and Ab initio calculations. *JETP Lett.* **91**, 143–146 (2010).
30. Dimiduk, D. M., Woodward, C., LeSar, R. & Uchic, M. D. Scale-free intermittent flow in crystal plasticity. *Science* **312**, 1188–1190 (2006).
31. Du, C., Maresca, F., Geers, M. G. D. & Hoefnagels, J. P. M. Ferrite slip system activation investigated by uniaxial micro-tensile tests and simulations. *Acta Mater.* **146**, 314–327 (2018).
32. Breen, A. J. *et al.* Solute hydrogen and deuterium observed at the near atomic scale in high-strength steel. *Acta Mater.* **188**, 108–120 (2020).
33. Kawakami, K. & Matsumiya, T. Ab-initio investigation of hydrogen trap state by cementite in bcc-Fe. *ISIJ Int.* **53**, 709–713 (2013).
34. McEniry, E. J., Hickel, T. & Neugebauer, J. Ab initio simulation of hydrogen-induced decohesion in cementite-containing microstructures. *Acta Mater.* **150**, 53–58 (2018).

## Methods

### Material production and heat treatment

The steel ingot was continuously casted by desulphurization, converter processing, refining in furnace, and vacuum degassing. The ingots were then heat-treated by pre-heating (< 900°C), heating (950 – 1020°C) and tempering (1080 – 1120°C) for a total of 8 hours. The steel sheets were then hot-rolled in 5 steps between 1100°C and 850°C to reduce the ingot thickness from 40 mm to 6 mm, followed by water-cooling to 600°C. The steel sheets were then slow cooled in a pit furnace at 350°C.

### TEM experiments

Pearlitic steel sheet samples of 10 × 10 × 1 mm were mechanical polished, followed by a dual 8-kV argon ion beam polishing at an angle of 5° for 45 minutes in a precision etching coating system (PECS, Gatan). After polishing, EBSD mapping was performed to identify suitable grains to prepare TEM samples with a zone-axis near [111] ferrite. A FIB lift-out then was performed to prepare transmission electron microscope (TEM) specimens by using a xenon ion beam in three steps: 30 kV-300 pA, 30 kV-30 pA, and 5 kV-30 pA, in a ThermoFisher G4 Hydra Plasma FIB-SEM (PFIB) equipped with an EBSD detector (Symmetry, Oxford Instruments). The same procedures were used for preparing the post-mortem TEM samples from the deformed pillars. The TEM sample was imaged by a Thermo-Fisher Themis-Z Double-corrected S/TEM at 300 kV. The convergence angle is 17.9 mrad, while the collection angle under HAADF and ABF are 38 – 200 and 9 – 35 mrad, respectively. The selected-area diffraction pattern was taken with a camera length of 200 mm in a JEOL JEM-2100 TEM at 200 kV. Geometric phase analysis was

conducted with a software package Strain++ (25). The ferrite lattice, far from the interface, was used as a reference to calculate the strain.

### **APT specimen preparation**

APT samples were prepared from 1×1×15 mm matchstick bars, starting with rough electropolishing using 25% perchloric acid in acetic acid at 10-30 V until two needle specimens from the middle of the bar samples. Fine polishing was then conducted in 2% perchloric acid in butoxyethanol under an optical microscope. Polishing was undertaken at 30 V until a neck forms near the apex, and then at 10 V until a new sharp tip was formed. The sharpened tips were then ion-milled in FIB annular milling in the PFIB to capture the lamellar cementite in the APT field-of-view, by using an in-situ annular milling process as illustrated in Extended Data Fig. 1 a ~45° inclined cementite lamella was targeted as it provides an optimized combination of data yield and spatial resolution of elemental mapping at the interface. Although the analysis direction (the z-direction along the length of the tip) gives the highest spatial resolution in APT analysis<sup>26</sup>, using this analysis direction (horizontal cementite in tips) resulted in high tip fracture rate and low data yield in voltage-mode APT. The ion milling began with a 30 kV-4 nA beam for locating the region of interest (ROI) in the tip, followed by a 30 kV-100 pA beam for finer operation, ending with a 2 kV-100 pA beam for final shaping, see Extended Data Fig. 1 for details.

### **Hydrogen/deuterium charging and subsequent sample handling**

Deuterium charging of APT tip samples was carried out by using 0.1 M NaOH in D<sub>2</sub>O for 30 seconds. The charged samples were then transferred using a cryogenic sample transfer (cryo-transfer) protocol described in the Supplementary Information of a previous work (21). The samples used for in-situ micro-compression tests were hydrogen-charged in the same charging rig by using 0.1 M NaOH in H<sub>2</sub>O for 1 hour. After a quick dusting, the hydrogen-charged samples were immediately loaded into a SEM (Ultra, Zeiss) for testing. The loading takes approximate 10 minutes. The in-situ compression test generally required 30 minutes to start and 4 hours to complete.

### **APT analysis**

The data in Fig. 1 was acquired by using a Local Electrode Atom Probe (LEAP 3000 Si, CAMECA), and the data in Fig. 3 was acquired by using a Local Electrode Atom Probe (LEAP 4000X Si, CAMECA) with a cryo-transfer suite. All APT experiments were conducted at a pulse frequency of 200 kHz, a specimen temperature of 50 K, and a pulse fraction of 20%. All APT reconstructions used the default algorithm in AP Suite (Version 6.1, CAMECA) with the settings of 57% detector efficiency and 1.65 image compression factor. The 1-D concentration profiles in Figs. 1 and 3 were obtained from cuboid ROIs with fixed bin width of 0.1 without bin overlaps. The ion labeling is shown in Extended Data Fig. 2 from (A) deuterium-charged and (B) deuterium-free specimens. Note the absence of 2 Da peak in uncharged data (B).

### **Micro-compression specimen fabrication**

Pearlitic micropillars were prepared as illustrated in Extended Data Fig. 3: (A) EBSD was conducted on the surface of a polished bulk specimen to identify grains with normal orientation parallel to  $\langle 110 \rangle_{\text{ferrite}}$ . (B) and (C) Rough annular trenching was carried out at 30 kV, 4 nA, in a pattern with an outer diameter of 15  $\mu\text{m}$  and an inner diameter of 3  $\mu\text{m}$ . (D) Due to the cementite-ferrite orientation relationship, lamellar cementite in the  $\{112\}$  planes of ferrite matrix can be obtained, (E) We selected the micropillars with uniform cementite lamellae that are 40-50 degrees inclined to the subsequent micro-compression direction, to allow interfacial slip to be the primary deformation mode. The final ion milling step used 30 kV-30 pA until the desired geometry was achieved.

### Micro-compression experiments

The in-situ micro-compression experiments were conducted in a Zeiss Ultra SEM operated at 5-30 kV. Compression was applied by a PI85 (Hysitron) nanoindenter with a diamond punch with a 2- $\mu\text{m}$ -diameter flat tip. Compression experiments were carried out in strain-control mode at a rate of 3 nm/s, which is equivalent to a quasi-static loading at a strain rate of  $10^{-3}$ . The loading and straining data and the sample geometry were used to calculate the data on the stress–strain curves. Resolved shear stress was used to account for the influence of inclined angles of the cementite lamellae on the mechanical measurement.

### Thermal desorption analyses

Thermal desorption analyses using the experimental setup detailed in referece<sup>35</sup> were conducted to study hydrogen desorption from bulk specimens. The tests were conducted at a heating rate of 400 °C per hour on  $10 \times 10 \times 1$  mm sheets of pearlitic steel samples with cleaned and polished surfaces. This specimen dimension is the same as for the bulk specimens for the micro-compression tests. As shown in Extended Data Fig. 5, three conditions were used to confirm the hydrogen content in the three specimens: i) uncharged reference sample (black) with 17 mass part per billion (mppb); ii) 60-minute hydrogen-charging followed by a 30-minute desorption in the TDS vacuum chamber (blue) with 137 mppb; and iii) 60-minute hydrogen-charging followed by a 4-hour desorption in the TDS vacuum chamber (red) with 35 mppb. The inserted figure displays a comparison between the cases of (iii) and (i) with a clear distinction in their hydrogen content.

### DFT simulations

DFT simulations were conducted by using the Vienna ab-initio simulation package (VASP)<sup>36</sup>. The simulations used the Perdew-Burke-Erzerhof (PBE) exchange-correlation functional<sup>37</sup> and projector augmented-wave (PAW)<sup>38</sup> pseudopotentials with Fe-3d<sup>7</sup>4s<sup>1</sup> and C-2s<sup>2</sup>2p<sup>2</sup> valence electrons and a plane wave basis set cutoff of 500 eV. The simulations included spin polarization to account for the magnetic moment of iron, and a Methessel-Paxton smearing of 0.1 eV. All structures were minimized until the energy change between three consecutive steps was below  $10^{-5}$  eV. The relaxed lattice parameters of cementite (assuming the *Pnma* space group definition) were  $a = 5.03 \text{ \AA}$ ,  $b = 6.71 \text{ \AA}$  and  $c = 4.48 \text{ \AA}$ , and that of ferrite was  $a = 2.83 \text{ \AA}$ .

Dilute carbon vacancies and hydrogen defects, and pairs of those defects, were simulated in a 192-atom supercell of cementite, built from a 2 x 2 x 3 replica of the *Pnma* unit cell, and a 128-atom supercell of ferrite, built from a 4 x 4 x 4 replica of the conventional bcc unit cell. K-point sampling for these supercells was through Monkhorst-Pack grids<sup>39</sup> of 4 x 3 x 2 and 4 x 4 x 4, respectively. For higher concentrations, we describe the system using configurational ensembles, which allows us to take into account the various hydrogen-vacancy and vacancy-vacancy complexes that may form in a hypo-stoichiometric carbide. The configurational ensembles were modelled with the aid of the Site-Occupation Disorder (SOD) algorithm,<sup>40</sup> using 64-atom 2x1x2 supercells of cementite, with a 4x5x4 k-point grid. This resulted in 128 independent configurations at the four stoichiometries considered (6.25%, 12.5%, 18.75% and 25%).

The formation energy,  $E_f$ , of a defect (e.g. a hydrogen interstitial atom or a carbon vacancy), was calculated as:

$$E_f = E(\text{host} + n \text{ defects}) - E(\text{host}) \pm n * \mu(\text{defect})$$

Where  $E(\text{host})$  is the DFT energy of a perfect supercell,  $E(\text{host} + \text{defect})$  is the DFT energy of the same supercell with an added defect, and  $\mu(\text{defect})$  is the chemical potential of any atoms added (-) or removed (+) from the perfect supercell to form the defect. For carbon vacancies,  $\mu(\text{C})$  was taken as the DFT energy of diamond (*Fd $\bar{3}m$* ), while for hydrogen interstitial atoms, to sidestep the limitation of DFT in modelling gaseous dimers,<sup>41,42</sup> the chemical potential was defined with respect to a dilute H atom in ferrite:

$$\mu(\text{H}) = E(\text{Fe}_{192}\text{H}) - E(\text{Fe}_{192})$$

As such, the defect formation energy for hydrogen defects is also the relative change in solution energy between cementite and ferrite,  $\Delta E_{\text{sol}}$ .

The calculated carbon vacancy formation energy in otherwise stoichiometric cementite is 0.65 eV, indicating that the process is endothermic. Considering APT evidence of hypo-stoichiometry of cementite, especially near the cementite/ferrite interface, we believe that carbon vacancies exist in the cementite matrix. Thus, we compute the formation energy of vacancies at higher concentrations, shown in Extended Data Fig. 8. The lowest energy configuration for each structure is used to investigate the trapping of hydrogen.

Extended Data Fig. 9a shows the binding energy between a single vacancy and a hydrogen atom as a function of distance, modelled in the larger 192-atom supercell. Hydrogen is attracted to vacancies that are within 3.5 Å, and is preferentially accommodated within the vacancy, where it is strongly bound (binding energy of 0.11 eV). The attraction is short-ranged, with the energy rapidly converging to that of dilute hydrogen in a perfect cementite. We further consider the hydrogen trapping behavior in the structures with higher vacancy concentrations by placing a hydrogen atom in every interstitial site of the lowest energy SOD configurations for each composition. The results are shown in Extended Data Fig. 9b. A wide range of solution energies is observed, depending on the local environment of the hydrogen atom in the hypo-stoichiometric cementite. At all concentrations, all states for hydrogen solution are lower energy than in the stoichiometric cementite, suggesting that vacancies have a strong trapping effect. The presence of 6.25% vacancies leads to a reduction in solution energy of up to 0.1 eV. Interestingly, at low

vacancy concentrations, hydrogen preferentially occupies the vacancy sites, while at higher vacancy concentration the interstitial sites become lower energy, with the cross-over occurring between 12.5–18.75%.

The interface of cementite is not only characterized by the presence of excess vacancies, but also by a biaxial strain field that accommodates the lattice mismatch in the coherent ferrite/cementite interface, as shown in our HAADF-STEM observations. The lattice mismatch between ferrite and cementite is 2.7% along  $[111]_{\text{ferrite}}//[010]_{\text{cementite}}$  and 0.8% along  $[\bar{1}\bar{1}0]_{\text{ferrite}}//[10\bar{1}]_{\text{cementite}}$ . We consider a range of strains for both materials, varying linearly between these values and zero strain. We rotate the strain matrix to align them to the coordinates of the conventional unit cells of ferrite and cementite, and then apply them to the  $\mathbb{I}c_{192}\mathbb{I}$  ferrite supercell and the lowest solution energy structures of cementite shown in Extended Data Fig. 9b.

We define the equilibrium lattice parameter at the interface,  $d_f^{\Delta\sigma=0}$  and  $d_c^{\Delta\sigma=0}$  for ferrite and cementite respectively, as those for which

$$\sigma_i^f = \sigma_i^c$$

thus,

$$\sum_j c_{ij}^f \varepsilon_j^f = \sum_j c_{ij}^c \varepsilon_j^c$$

With the DFT-derived elastic constants of ferrite and cementite (see Extended Data Table 3), this equates to a 56% of the total strain being accommodated in ferrite, and the resulting lattice spacing on the habit plane of the interface are reported in Extended Data Table 4. The deviation in strain from this equilibrium interface biaxial strain is defined as

$$\Delta\mathcal{E}_{\text{interface}} = \frac{d_1 - d_1^{\Delta\sigma=0}}{d_1^{\Delta\sigma=0}} + \frac{d_2 - d_2^{\Delta\sigma=0}}{d_2^{\Delta\sigma=0}}$$

where  $d_1$  and  $d_2$  refer to  $[111]_{\text{ferrite}}//[010]_{\text{cementite}}$  and  $[\bar{1}\bar{1}0]_{\text{ferrite}}//[10\bar{1}]_{\text{cementite}}$ , respectively.

Extended Data Fig. 9c shows that in both materials biaxial compression increases the solution energy, while tension decreases it. In practice this means that the interfacial strain leads to a decrease in hydrogen solution energy in ferrite as H approaches the interface from bulk ferrite, and an increment in solution energy in cementite as H approaches the interface from bulk cementite. The presence of vacancies has an even stronger effect on the reduction of hydrogen solution energy, overwhelming the effect of strain in cementite.

**Data and Code Availability:** The data that support the findings of this study are available from the corresponding author upon reasonable request.

## References for methods

35. Lin, Y. C. et al. Hydrogen trapping and desorption of dual precipitates in tempered low-carbon martensitic steel. *Acta Mater.***196**, 516–527 (2020).
36. Kresse, G. & Furthmüller, J. Efficiency of ab-initio total energy calculations for metals and semiconductors using a plane-wave basis set. *Comput. Mater. Sci.***6**, 15–50 (1996).
37. Perdew, J. P., Burke, K. & Ernzerhof, M. Generalized gradient approximation made simple. *Phys. Rev. Lett.* **77**, 3865–3868 (1996).
38. Blöchl, P. E. Projector augmented-wave method. *Phys. Rev. B***50**, 17953–17979 (1994).
39. Monkhorst, H. J. & Pack, J. D. Special points for Brillouin-zone integrations. *Phys. Rev. B***13**, 5188 (1976).
40. Grau-Crespo, R., Hamad, S., Catlow, C. R. A. & De Leeuw, N. H. Symmetry-adapted configurational modelling of fractional site occupancy in solids. *J. Phys. Condens. Matter***19**, (2007).
41. Burr, P. A., Murphy, S. T., Lumley, S. C., Wenman, M. R. & Grimes, R. W. Hydrogen accommodation in Zr second phase particles: Implications for H pick-up and hydriding of Zircaloy-2 and Zircaloy-4. *Corros. Sci.***69**, 1–4 (2013).
42. Lozovoi, A. Y., Alavi, A. & Finnis, M. W. Surface energy and the early stages of oxidation of NiAl(110). *Comput. Phys. Commun.***137**, 174–194 (2001).

## Declarations

**Acknowledgments:** A. Breen, H.W. Liu, V. Bhatia, T. Sato, S.Y. Huang, N. Holmes, and H.S. Chen (The University of Sydney) are thanked for their technical supports. D.G. Xie (Xi'an Jiao Tong University) is thanked for useful discussion. Y.-S. C. thanks his family.

**Funding:** The authors acknowledge funding from Australian Research Council Linkage Project (LP180100431), Future Fellowship (FT180100232), the 2019 University of Sydney Postdoctoral Fellowship, CITIC-CBMM Nb Steel Award Fund Program (2018FWNB30064), Taiwan's Ministry of Science and Technology (MOST 110-2119-M-002 -018 -MBK), USyd-NTU Partnership Award, and China Scholarship Council (201506840096). The authors also thank the research facilities supported by Microscopy Australia, the University of Sydney, the Australian National Computational Infrastructure, the Pawsey Supercomputing Centre, and Intersect Australia Limited.

## Author contributions:

Conceptualization: YSC, RMN, JMC, HZL. Methodology: RMN, YSC, PB, HYL, PYL. Investigation: RMN, YSC, PB, HYL, PYL, JMC, HWY. Materials synthesis: YF, HZL, MTM. Data visualization: RMN, YSC, HYL,

PYL, PB. Funding acquisition: JMC, YSC, HZL, AMG. Project administration: YSC, JMC, HZL. Supervision: JMC, YSC, RMN, PB, AMG, HZL, MTM, HWY. Manuscript writing: RMN, YSC. Manuscript editing: JMC, PB.

**Competing interests:** All authors declare no competing interests.

**Additional information:**

**Supplementary information** is available for this paper.

Correspondence and requests for materials should be addressed to Julie M. Cairney, Yi-Sheng Chen and Hongzhou Lu.

**Peer review information** *Nature* thanks the reviewer(s) for their contribution to the peer review of this work. Peer reviewer reports are available.

**Reprints and permissions information** is available at [www.nature.com/reprints](http://www.nature.com/reprints).

## Figures

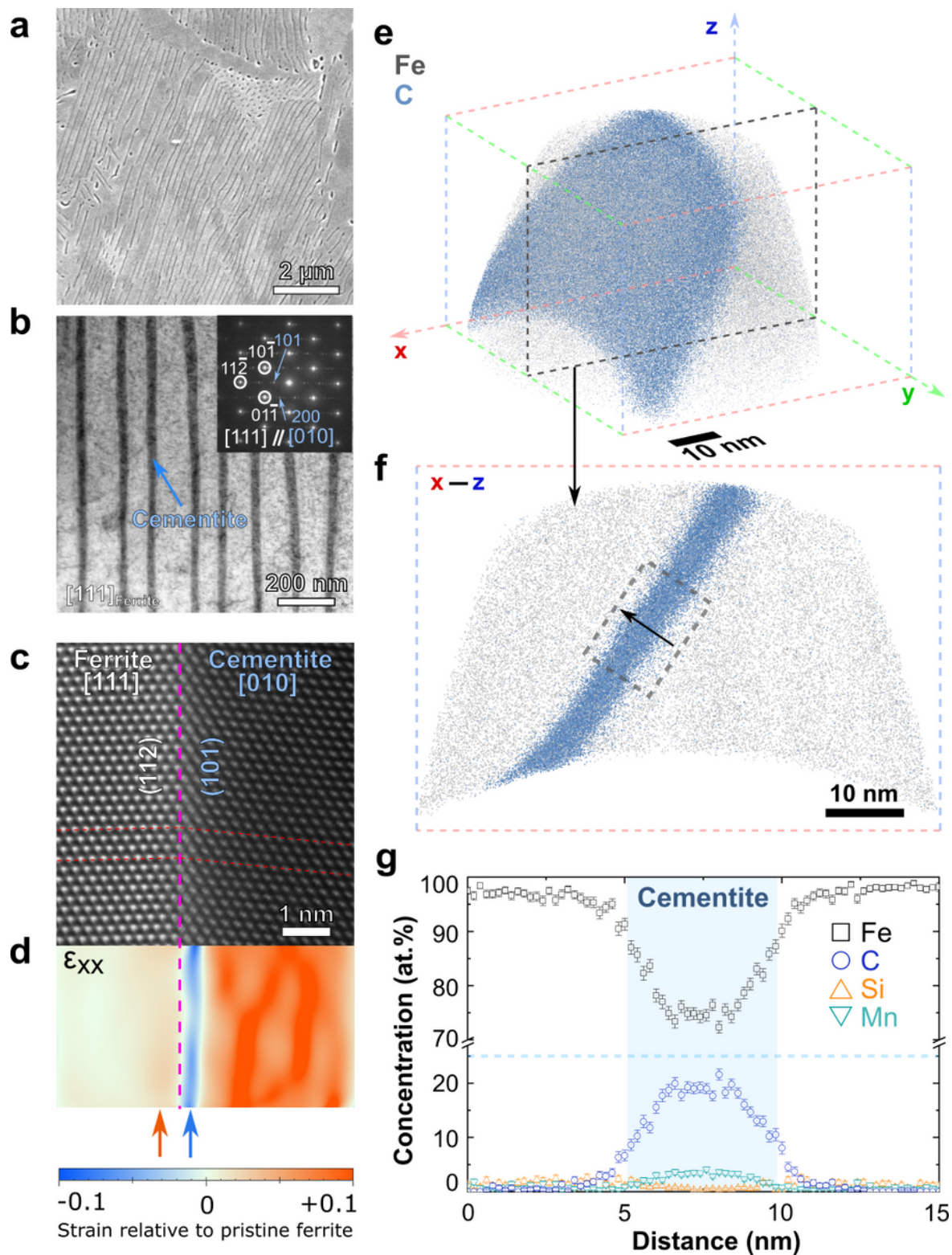
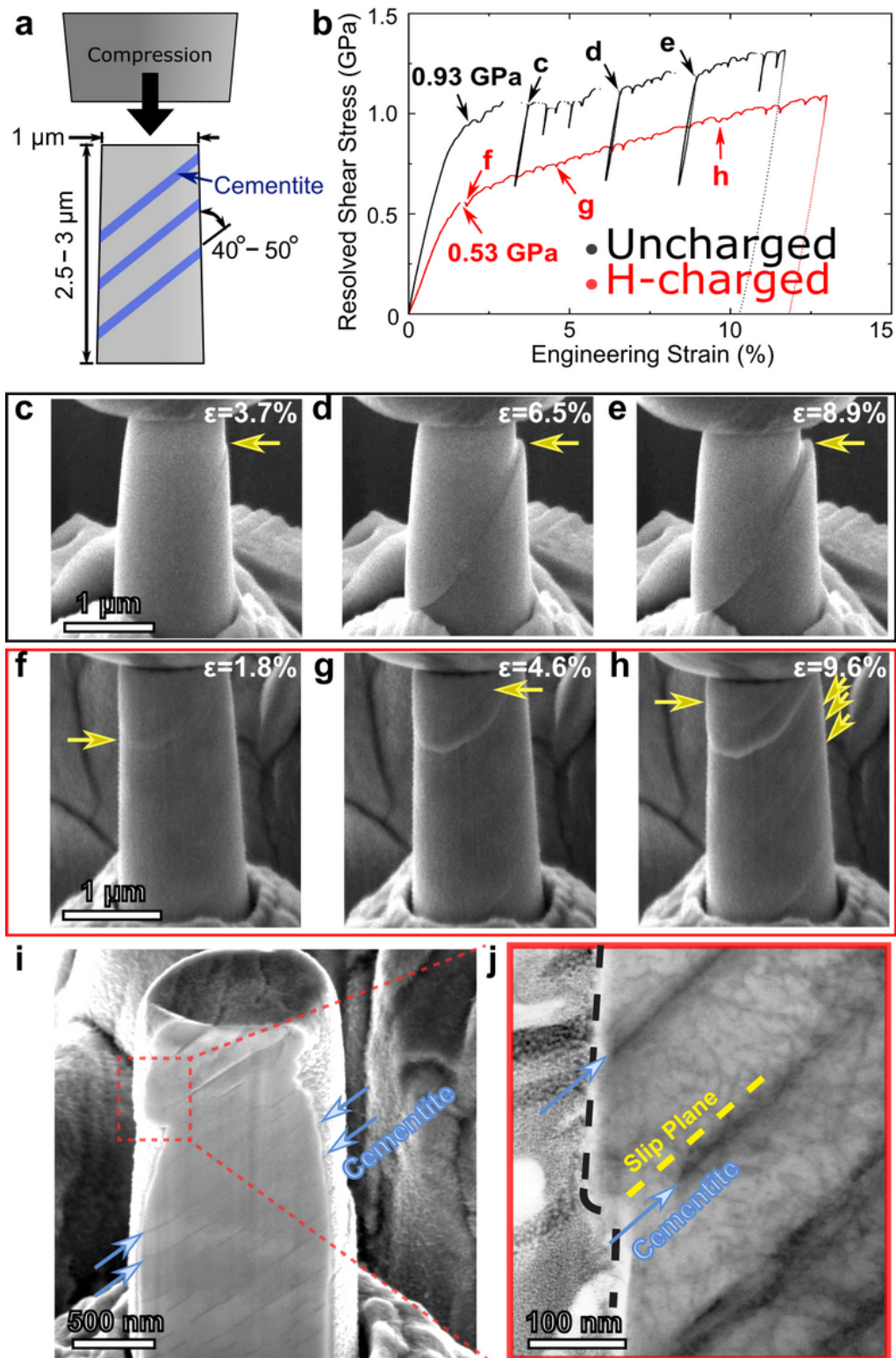


Figure 1

**As-received pearlitic steel specimen.** (a) Secondary electron scanning electron microscopy (SEM) image and (b) bright-field TEM image showing the pearlitic microstructure containing lamellar cementite. The inset selective area electron diffraction pattern in (b) and the atomic resolution HAADF-STEM image in (c) show that the ferrite and cementite are coherent. (d) is a strain map obtained from (c) by using geometric phase analysis, showing an expansion (orange arrow) of the ferrite lattice and a compression (blue

arrow) of cementite near the interface. Positive and negative strain values correspond to tension and compression, respectively. (e) is an APT 3-D atom map reconstruction with iron (grey) and carbon (blue). (f) is a 10-nm thick slice from the region marked by the broken line in (e). (g) is a 1-D concentration profile from the region of interest in (e) along the direction marked with an arrow. The carbon (max 22.32 at.%) in the cementite is lower than the stoichiometric value ( $\text{Fe}_3\text{C}$ ), in company with modest manganese (2.34 at.%) and silicon (0.22 at.%). The bulk composition of this dataset is C - 0.06 at.%, Mn - 1.26 at.%, and Si - 0.58 at.%.



**Figure 2**

**In-situ micromechanical testing and post-mortem imaging.** (a) A schematic of the experimental configuration for the micro-compression test. (b) Engineering shear strength of uncharged (black) and hydrogen-charged (red) micropillars as a function of their nominal strain. (c), (d), (e) are still images from Supplementary Video 2 at the instants noted in (b), showing the deformation of the uncharged pillar. (f), (g), (h) are from the hydrogen-charged pillar, taken from Supplementary Video 3. The yellow arrows in the

figures indicate slip bands at the given strain levels. (i) is an SEM image of a cross-section of the deformed and hydrogen-charged micropillar after FIB milling. (j) is a STEM image from the region highlighted in (i), showing that the slip occurs within the ferrite strain, not at the interface itself.

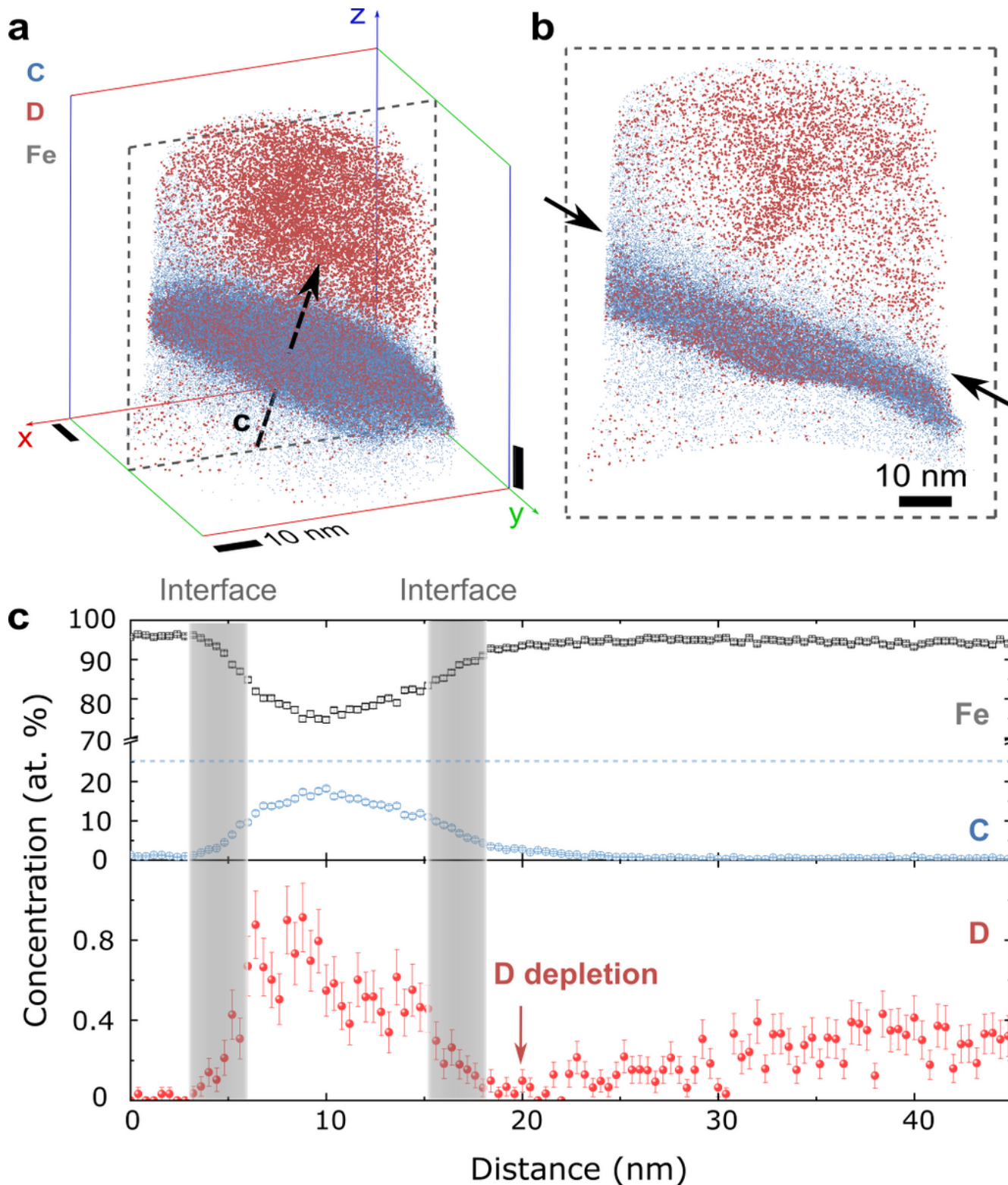
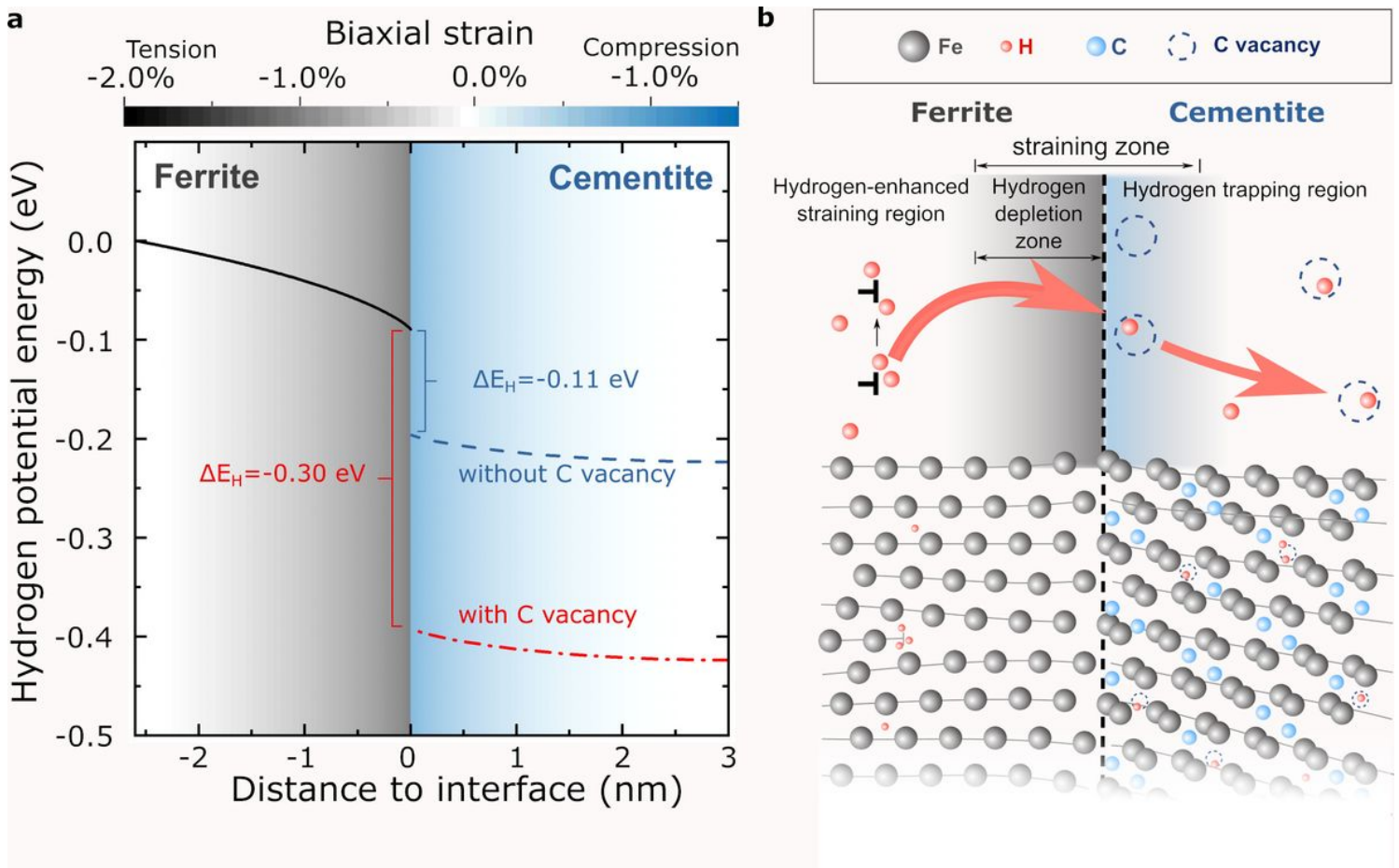


Figure 3

**APT analysis of deuterium-charged pearlitic specimen.** (a) is a reconstructed 3-D atom map showing the spatial distribution of carbon (blue), deuterium (red), and iron (grey). (b) is a 20-nm thick slice from the region highlighted by broken line in (a), showing that the deuterium is concentrated in the cementite and ferrite bulks, but appears to be depleted near the cementite–ferrite interface. (c) is a 1-D concentration profile from the region highlighted in (b), showing that the cementite is rich in deuterium, and confirming the existence of the deuterium depletion zone.



**Figure 4**

**Hydrogen behavior around the cementite–ferrite interface.** (a) DFT-calculated hydrogen potential energy near the cementite–ferrite interface and (b) a schematic illustration of hydrogen migration and trapping. The gradient colors of grey and blue indicate the strain gradient with respect to distance from the ferrite/cementite interface. The blue and red broken lines delineate the hydrogen potential energy in cementite with 0 and 6.25 at.% carbon vacancies, respectively. (b) illustrates hydrogen-dislocation interactions in ferrite bulk, hydrogen depletion in ferrite due to a lower potential energy in cementite, the carbon vacancy hydrogen trapping in cementite, and the incorporation of hydrogen inside the cementite phase due to the lower potential energy in the relaxed cementite lattice away from the interface.

# Supplementary Files

This is a list of supplementary files associated with this preprint. Click to download.

- [ExtendedDataFig.1.png](#)
- [ExtendedDataFig.2.png](#)
- [ExtendedDataFig.3.png](#)
- [ExtendedDataFig.4.png](#)
- [ExtendedDataFig.5.png](#)
- [ExtendedDataFig.6.png](#)
- [ExtendedDataFig.7.png](#)
- [ExtendedDataFig.8.png](#)
- [ExtendedDataFig.9.png](#)
- [ExtendedDataTables.docx](#)
- [SupplementaryVideo1.mp4](#)
- [SupplementaryVideo2.mp4](#)
- [SupplementaryVideo3.mp4](#)
- [SupplementaryVideo4.mp4](#)
- [SupplementaryVideo5.mp4](#)